PAPER

Check for updates

Structural, vibrational, photoelectrochemical, and optical properties of two-dimensional Ruddlesden–Popper perovskite BA$_2$PbI$_4$ crystals†

Aochen Du, [ID] [a,b] Debing Shen,[c] Wenxiao Zhao,[a,b] Yongzhen Liu,[a,b] Xinzhi Qin,[a,b] Zexi Lin,[a,b] Yun Ye,*[a,b] Enguo Chen, [ID] *[a,b] Sheng Xu[a,b] and Tailiang Guo[a,b]

Two-dimensional organic–inorganic hybrid Ruddlesden–Popper perovskites have attracted a lot of attention due to their unique photochemical properties and enhanced stability towards photoluminescence devices. Compared with three-dimensional materials, two-dimensional perovskites show great potential for photoelectric applications due to their tunable band gap, great excitation binding energy, and large crystal anisotropy. Although the synthesis and optical properties of BA$_2$PbI$_4$ crystals have been extensively studied, the role of their microstructure in photoelectric applications, their electronic structure, and their electron–phonon interaction are still poorly understood. In this paper, based on the preparation of BA$_2$PbI$_4$ crystals, the electronic structure, phonon dispersion, and vibrational properties of BA$_2$PbI$_4$ crystals were revealed in detail with the help of density functional theory. The BA$_2$PbI$_4$ stability diagram of formation enthalpy was calculated. The crystal structure of the BA$_2$PbI$_4$ crystals was characterized and calculated with the aid of Rietveld refinement. A contactless fixed-point lighting device was designed based on the principle of an electromagnetic induction coil, and the points with different thicknesses of BA$_2$PbI$_4$ crystal were tested. It is proved that the excitation peak of the bulk is 564 nm, and the surface luminescence peak is 520 nm. Phonon dispersion curves and the total and partial phonon densities of states have been calculated for the BA$_2$PbI$_4$ crystals. The calculated results are in good agreement with the experimental Fourier infrared spectra. Besides the basic characterization of the BA$_2$PbI$_4$ crystals, the photoelectrochemical properties of the materials were also studied, which further proves the excellent photoelectric properties of the BA$_2$PbI$_4$ crystals and the broad application prospect.

Introduction

In recent years, novel thin film optoelectronic devices based on three-dimensional (3D) organic inorganic halide perovskites have been developed rapidly. They have excellent optical and electronic properties, such as strong light harvesting ability, excellent charge transportation, high defect tolerance, and excellent solution processing performance.[1–5] However, their innate instabilities over moisture, light, and heat remain key obstacles to achieve commercial, large-scale production applications.[6–9] In contrast, the emerging two-dimensional (2D) Ruddlesden–Popper perovskites have attracted more and

more attention due to their superior environmental stability and large exciton binding energies, and continuous adjustability of their optoelectronic properties and great potential in the fields of light-emitting diodes, solar cells, photodetectors, and lasers.[10–12] Two-dimensional (2D) layered hybrid perovskite quantum well materials, whose chemical formula is generally $(C_nH_{2n+1}NH_3)_2(CH_3NH_3)_{m-1}Pb_mX_{3m+1}$ (X = Cl, Br, I; m = 1, 2...; n = 1, 2...), consist of a lead halide layer inserted between the organic barrier surfaces.[13–15] In 2D perovskite semiconductors, the van der Waals interaction between organic cations and inorganic anions is very large and requires more energy to destroy the 2D crystal structure. Compared with 3D perovskites, 2D perovskites have better stability. In an experiment, Yang *et al.* reported for the first time the colloid synthesis of a single-crystal 2D perovskite BA$_2$PbBr$_4$, confirming the existence of a 2D perovskite by separating a single layer of PbBr$_4^-$.[16] Theoretically, Liu *et al.* explored the electronic structure and optical properties of MA$_2$PbI$_4$, indicating that the 2D film can be used as an efficient solar absorber.[17] Zeng *et al.* studied single-layer BA$_2$GeI$_4$ and BA$_2$SnI$_4$, indicating their potential

aCollege of Physics and Information Engineering, Fuzhou University, Fuzhou 350100, China. E-mail: yeyun07@fzu.edu.cn, ceg@fzu.edu.cn

bFujian Science & Technology Innovation Laboratory for Optoelectronic Information of China, Fuzhou 350100, China

cCollege of Chemistry, Fuzhou University, Fuzhou 350100, Fujian, China

†Electronic supplementary information (ESI) available. See DOI: https://doi.org/10.1039/d2nr06860e

applications in photovoltaic or light-emitting devices due to their appropriate band gap and exciton effects.[18,19] In previous studies, when BA_2PbI_4 crystals were excited at different angles, the two emission peaks of the emission spectrum show different proportions. This is attributed to the difference in the depth of excitation light intake and the difference in the emission spectra between the bulk and the surface at different angles.[20,21]

As mentioned above, 2D Ruddlesden–Popper perovskites are very suitable for photoelectric applications. BA_2PbI_4 is a kind of simple and stable 2D perovskite, which shows rich excitonic photophysics in the visible light region. Perovskite BA_2PbI_4 crystals have attracted significant attention in the field of photoelectric device (such as PLEDs, solar cells, *etc.*) research due to their excellent photoelectronic properties. It has become a research hotspot for the following reasons. (1) High absorption coefficient: BA_2PbI_4 has a high absorption coefficient, which means it can absorb a significant amount of light, even with a thin film. This makes it an excellent material for using in solar cells. (2) Wide bandgap: the wide bandgap of BA_2PbI_4 makes it suitable for absorbing a large portion of the solar spectrum, which is important for solar cell efficiency. (3) Low toxicity: unlike other lead-based materials, BA_2PbI_4 has a low toxicity, which makes it more environmentally friendly. (4) Stability: perovskite BA_2PbI_4 is thermally stable, making it more resistant to degradation under light and heat. (5) Simple synthesis: the synthesis of BA_2PbI_4 crystals is relatively simple, which makes it an attractive option for large-scale production. Overall, perovskite BA_2PbI_4 crystals offer a promising alternative to traditional silicon solar cells due to their high efficiency and low-cost fabrication. Therefore, BA_2PbI_4 is a good research target to reveal the photoelectric characteristics of 2D Ruddlesden–Popper perovskites. In this paper, BA_2PbI_4 crystals with a nanorod microstructure were successfully prepared. The crystal structure of the BA_2PbI_4 crystals was studied by Rietveld refining of the XRD and diffraction calibration of SAED. The micro morphology of BA_2PbI_4 crystals was studied by SEM and TEM, and the electric field generated by spherical and cylindrical microstructures was studied by the finite element method. A contactless fixed-point lighting device was designed based on the principle of an electromagnetic induction coil, and the points with different thicknesses of the BA_2PbI_4 crystals were tested. The electronic structure of the BA_2PbI_4 crystals was studied by first-principles calculations. The phonon relaxation and vibrational properties were also studied. Finally, the photoelectrochemical properties of the BA_2PbI_4 crystals were studied by Mott–Schottky analysis, transient photocurrent responses, and electrochemical impedance spectroscopy.

Experiment

Synthesis method

10 mmol of *n*-$C_4H_9NH_2$ solution was mixed with 38 mmol of 57% w/w HI, and the BAI solution was obtained after stirring constantly in an ice bath for 4 hours. By heating to boiling under constant magnetic stirring, 10 mmol of PbO was dissolved in a mixture of 76 mmol of 57% w/w HI aqueous solution and 15.5 mmol of 50% aqueous H_3PO_2 solution to obtain a bright yellow solution. The newly prepared BAI was added into this solution, and the resulting solution was heated to boiling. Stirring was immediately stopped after boiling and the solution was cooled to room temperature. During the cooling process, the orange coloured plate-like crystals started to crystallize. The crystals were filtered and washed with diethyl ether and dried under vacuum.

Characterization

Structural analysis of the BA_2PbI_4 crystals was carried out using powder X-ray diffraction (PXRD, PANalytical, X'pert Highscore Plus, Netherlands) measurements with a Cu Kα radiation source (λ = 1.54 Å generated at 40 kV and 40 mA). The microstructure of the sample was observed using a field emission scanning electron microscope equipped with an energy dispersive spectrometer (FESEM + EDS, FEI, Nova NanoSEM 230, USA) and a transmission electron microscope (TEM, FEI, Tecnai G2 F20, USA). The optical properties were studied by using a UV-Vis-NIR spectrometer (UV-Vis, Hitachi U-4100, Japan) and a photoluminescence spectrometer (PL, Ocean Insight, QEPro). The PL spectra were measured along the optical fiber placed at different angles from the BA_2PbI_4 crystals. Tesla coils used in the contactless electroluminescence devices were produced by Wuhan Stark Technology Co., Ltd. Mott–Schottky (M–S) analysis, transient photocurrent responses (TPR), and electrochemical impedance spectroscopy (EIS) for evaluating photoelectrochemical properties were performed using an electrochemical workstation (CHI 660E, China). An aqueous solution of Na_2SO_4 (0.5 mol L^{-1}) and lactic acid (10%, v/v) served as the electrolyte. Incandescent lamps under visible light were used in all electrochemical tests. 5 mg of the photocatalyst was suspended in a solution mixture of ethanol and Nafion.
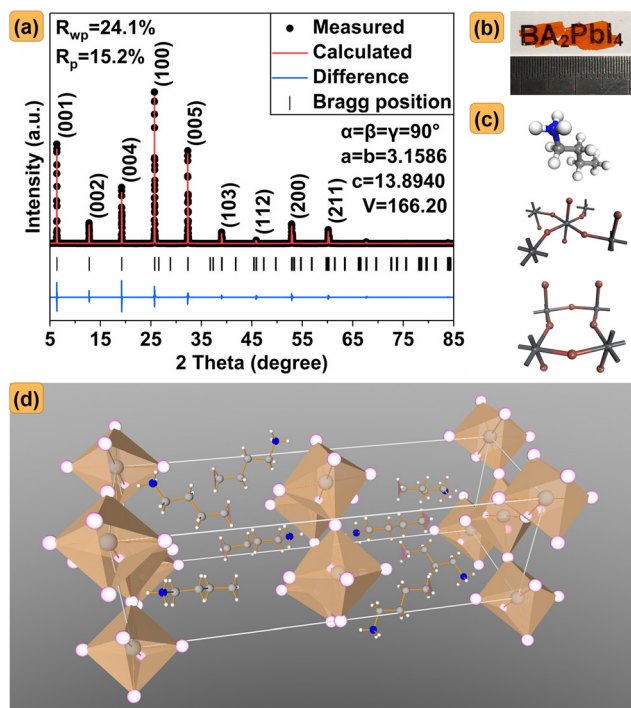
Calculation

Based on density functional theory (DFT), the Kohn–Sham equation was calculated using the robust technique of a plane-wave basis set and the pseudopotential method was used to study the electronic structure, phonon relaxation, and vibrational properties of BA_2PbI_4. The electron exchange related effects were approximated by the generalized gradient approximation using the Perdew–Burke–Ernzerhof (GGA-PBE) functional and the interaction of electron ions was studied using the ultrasonic pseudopotential (USP) method.[22] The hybrid potential Heyd–Scuseria–Ernzerhof (Hybrid-HSE06) was also considered to evaluate more accurate band gap. The pseudopotential method implemented in CASTEP provides efficient and fast computation due to the non-priori nature of the initial shape approximation of atomic orbitals. Electronic wave functions were expanded by using a plane-wave basis set with an optimized cut-off energy (E_{cut}) of 500 eV. The ground state energy structure was obtained by geometric optimization through a single-point energy calculation. In the geometric

optimization step, the atomic position and lattice parameters were iteratively refined in a mixed space of element internal parameters and element degrees of freedom. Electronic wave functions were expanded by using a plane-wave basis set with an optimized cut-off energy (E_{cut}) of 500 eV. Brillouin zone integration was performed using a $3 \times 3 \times 1$ k-mesh. All the calculations have converged on the energy convergence standard 10^{-5} eV and the force convergence standard 0.01 eV Å^{-1} per atom. Then the electronic structure, phonon relaxation, and vibrational properties of BA_2PbI_4 were calculated by using the optimized structure.

Results and discussion

Crystal structure

Due to different preferred orientations, PXRD patterns only reflect the diffraction peaks of $(0\ 0\ L)$ ($L = 2, 4, 6, 8, 10, 12,$ and 14) crystal planes, as shown in Fig. 1(a), which also reveals a layered structure.[23,24] The BA_2PbI_4 crystals are confirmed to be a pure phase by the Rietveld refining method. Fig. 1(b) shows an optical image of the synthesized perovskite BA_2PbI_4 crystals under sunlight. The crystal structure of BA_2PbI_4 is shown in Fig. 1(d). The crystal structure space group belongs to *Pbca*, and the orthorhombic BA_2PbI_4 layered perovskite structure consists of an extended two-dimensional perovskite structure with an angle shared PbI_6 octahedron, the octahedron center is Pb, and the coordination atom is iodine as shown in Fig. 1(c). Twisted PbI_6 octahedral single-layer perovskite flakes alternate with the protonated n-$C_4H_9NH_2$ cation bilayer. For the organic–inorganic hybrid perovskite compound BA_2PbI_4, specific chemical interactions in solution include relatively weak van der Waals interactions between the n-$C_4H_9NH_2$ cation bilayers, hydrogen bonding interactions between the n-$C_4H_9NH_2$ cation and the inorganic component PbI_6 octahedron, and stronger ion covalent interactions in the PbI_6 octahedron sheet.[25] Details of the atomic distance atomic parameters are shown in Tables S1 and S2.† This structural property provides many advantages, such as high ionic mobility and thermal stability, which makes BA_2PbI_4 crystals possible to be used in photoelectronic applications.
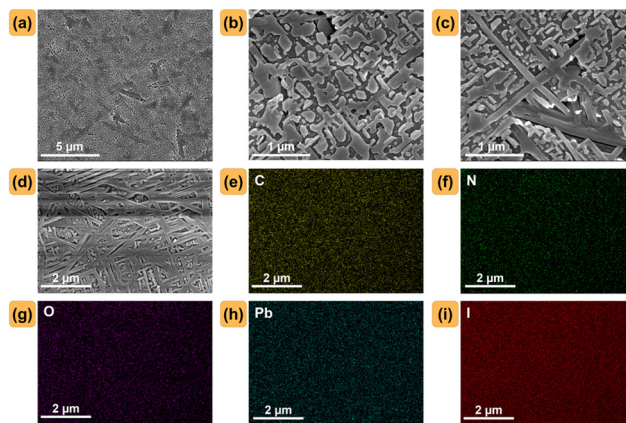
Microstructure

The microstructure within the materials will not only affect the stability and practicality, but also affect the photoelectric properties of the materials. In order to study the microstructure, the BA_2PbI_4 crystals were studied by SEM (Fig. 2) and TEM (Fig. 3). The SEM images of the BA_2PbI_4 crystals show a nanorod microstructure (Fig. 2(a)–(d)), and the EDS mapping shows that C, N, O, Pb and I elements are uniformly distributed in the BA_2PbI_4 crystals (Fig. 2(e)–(i)). Fig. 3 shows TEM morphologies of the BA_2PbI_4 crystals. Obviously, the microstructure exhibits a rod-like structure with a single crystalline phase. The diameter of a single nanorod is about 200 nm, and the length varies from hundreds of nanometers to tens of microns. Analysis of the SAED patterns shows that these nanorods are single crystals with a cubic organic metal halide perovskite. The diffraction ring in Fig. 3(f) demonstrates the existence of the R_1 (2 1 4), R_2 (2 2 3), R_3 (0 4 1), R_4 (3 3 5), R_5 (4 3 5) and R_6 (1 6 6) crystal planes of BA_2PbI_4 crystals.

Phase stability diagram

Under thermodynamic equilibrium growth conditions, the existence of BA_2PbI_4 should satisfy the following equation:[26]

$$2\mu_{BA} + \mu_{Pb} + 4\mu_I = \Delta H(BA_2PbI_4) = -9.577 \text{ eV} \qquad (1)$$

Fig. 1 (a) Rietveld refinement patterns of BA_2PbI_4. (b) Image of BA_2PbI_4 crystals under sunlight. (c) and (d) Crystal structures of BA_2PbI_4 showing the coordination environments of BA, Pb and I.

Fig. 2 (a–d) SEM images for the edge area of BA_2PbI_4 crystals. (e–i) EDS mapping images of (d).
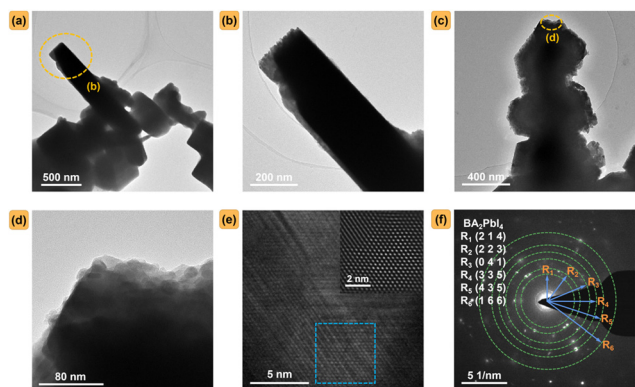
Fig. 3 (a–d) TEM images, (e) HRTEM image and (f) SAED pattern of BA$_2$PbI$_4$ crystals.

where μ_i (i = BA, Pb, I) is the chemical potential of the constituent element referred to its most stable phase and $\Delta(BA_2PbI_4)$ is the formation enthalpy of BA$_2$PbI$_4$. To exclude the possible secondary phases PbI$_2$ and BAI, the following constraints must also be satisfied:

$$\mu_{BA} + \mu_I \; < \; \Delta H(BAI) = -2.821 \text{ eV} \qquad (2)$$

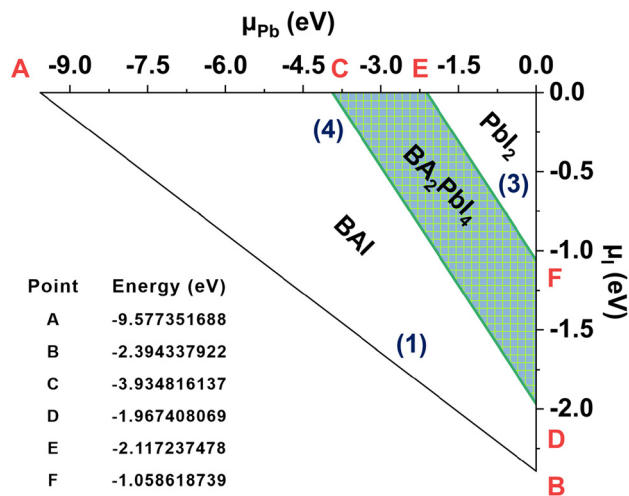$$\mu_{Pb} + 2\mu_I \; < \; \Delta H(PbI_2) = -2.117 \text{ eV} \qquad (3)$$

$$\mu_{Pb} + 2\mu_I \; > \; \Delta H(BA_2PbI_4) - 2\Delta H(BAI) = -3.935 \text{ eV} \qquad (4)$$

Eqn (4) is obtained by subtracting twice eqn (2) from eqn (1). The chemical potentials of Pb and I satisfying eqn (1)–(4) are shown as the green region in Fig. 4 (the preparation process shown in Fig. 4 has been presented in the ESI†). This chemical range indicates the growth conditions for synthesizing the BA$_2$PbI$_4$ phase under the equilibrium conditions. The shape is consistent with the low calculated dissociation energy (644.488 eV) of BA$_2$PbI$_4$ to BAI and PbI$_2$, defined as $E(BAI) + E(PbI_2) - E(BA_2PbI_4)$, which indicates that the growth conditions should be controlled to form the stoichiometric BA$_2$PbI$_4$ perovskite phase.
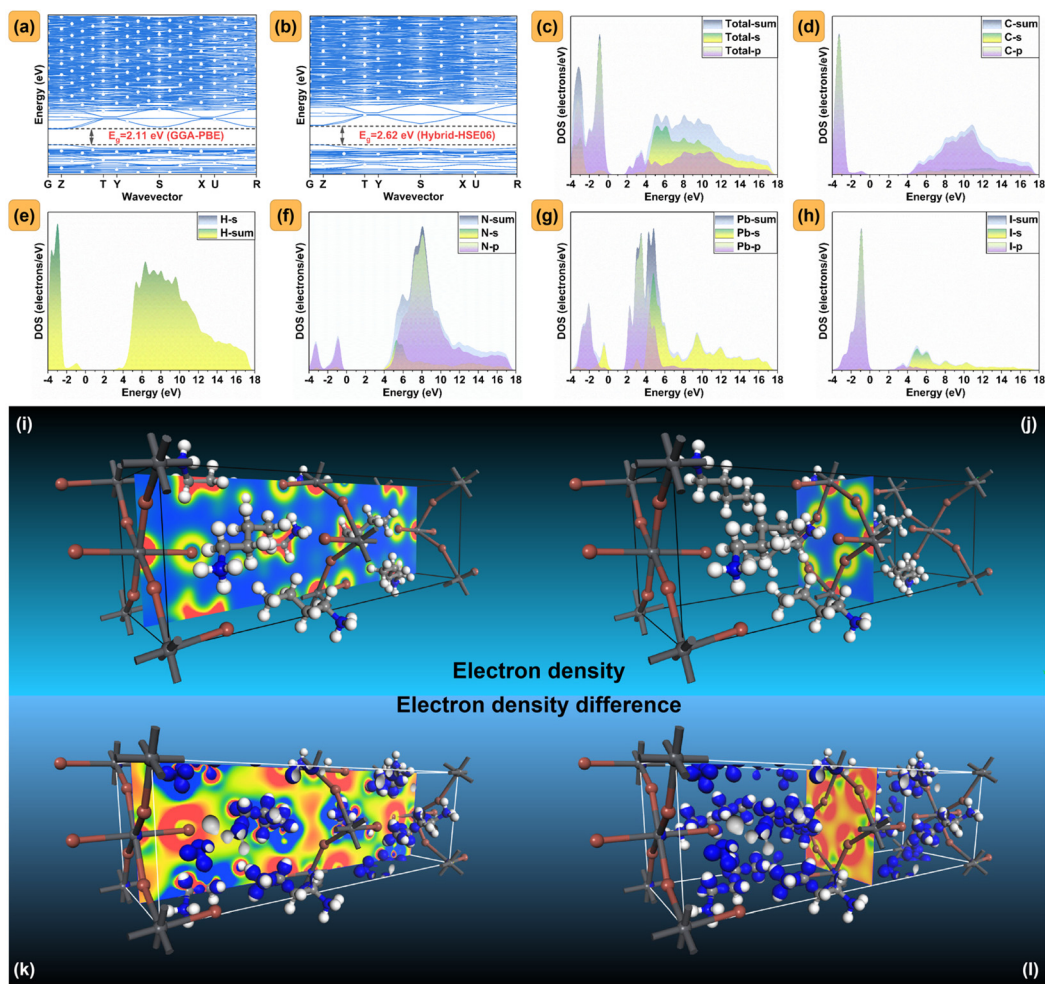
Electronic structure

As an effective tool to determine the structure of materials, first-principles calculations were used to study electronic properties and band structures. The electronic structure of BA$_2$PbI$_4$ was calculated after structural optimization through DFT calculations, and the corresponding band structure was calculated. As shown in Fig. 5(a) and (b), the results show that the direct band gaps (E_g) of BA$_2$PbI$_4$ are about 2.11 eV (GGA-PBE) and 2.62 eV (hybrid-HSE06). The reason is that the maximum value of the valence band and the minimum value of the conduction band are located at the same G point. The GGA-PBE functional describes the exchange energy and calculates the system energy more accurately. Moreover, GGA-PBE is the most popular functional in the calculation of perovskites and has been widely used in many papers.[9,18,21] Therefore, the description of the electronic structure is based on the results

Point	Energy (eV)
A	-9.577351688
B	-2.394337922
C	-3.934816137
D	-1.967408069
E	-2.117237478
F	-1.058618739

Reference state	Energy	Unit cell number	Energy/Unit cell number	
Pb	-14.22196064	4	-3.55549016	
I	-2.93993087	2	-1.469965435	
BA	-86.73996679	1	-86.73996679	

Phase	Energy	Unit cell number	Energy/Unit cell number	ΔH
PbI$_2$	-34.45063403	4	-8.612658508	-2.117237478
BAI	-91.0312	1	-91.0312	-2.821267775
BA$_2$PbI$_4$	-769.9705487	4	-192.4926372	-9.577351688

Fig. 4 Phase stability diagram of BA$_2$PbI$_4$.

of GGA-PBE functional calculations. Since the GGA-PBE functional always underestimates the band gap, the hybrid-HSE06 functional is also used to calculate the band gap. The total density of states (TDOS) and partial density of states (PDOS) of BA$_2$PbI$_4$ are shown in Fig. 5(c)–(h). These characteristics can be used to understand the composition of the energy band. It is observed that the top of the valence band (VB) is dominated by the I (5p) state, while the bottom of the conduction band (CB) is mainly formed by the Pb (6p) state. As discussed previously, the host absorption of the BA$_2$PbI$_4$ crystals can be mainly ascribed to the charge transitions from the I (5p) state to the Pb (6p) state. The different characteristics of the valence and conduction band edge states imply high ionizability, which is similar to the properties of other Pb-based perovskites, including a direct band gap at point G and a relatively small effective mass. The valence bands (VBs) consist of Pb (6s)–I (5p) antibonding states, nonbonding I (5p) states, and Pb (6p)–I (5p) states with their band widths calculated to be 1.054, 1.503, and 2.054 eV, respectively. Below the valence band, it is found that the positions of the I (5p) state and Pb (6s) state are between −7.02 eV and −8.06 eV, while the Pb (6p) state and I (5s) antibonding state are also in the same range, but the positions are relatively low, and they basically do not contribute to the valence band. In addition, the lowest unoccupied state is mainly composed of Pb (6p)–I (5s) antibonding and Pb (6p)–I (5p) antibonding states. In addition, the PDOS

Fig. 5 (a) and (b) Band structures (GGA-PBE and hybrid-HSE06), (c)–(h) densities of states, (i) and (j) electron densities, and (k) and (l) electron density differences of BA_2PbI_4.

diagram shows that the states between C (2s2p) and N (2s2p) almost completely overlap, except that there is a peak near the Fermi level, while the H (1s) state almost overlaps with the C (2p) and N (2p) states. This shows that there is a strong covalent interaction between the C–H and N–H bonds in the structure. Regarding the outstanding photoelectric character-istics of a two-dimensional halide perovskite, it should come from two aspects, one is the direct band gap that can effec-tively utilize power generation tubes without phonon assist-ance, and the other is the effective electron transfer of p–p transitions, a lone-pair s electron. Since the p orbital has two more orbitals than the s orbital and the dispersion is small, the p–p transition of the direct band gap is usually much larger than the s–p transition. These conclusions are highly consistent with previous studies.[17] Fig. 5(i)–(l) show the elec-tron density and electron density difference for BA_2PbI_4 at different sections. The electron density difference is the charge density difference between the superposition of self-consistent pseudo charge density and atomic charge density. Negative charge density means the loss of electrons, and positive charge

density means the acquisition of electrons. It can be seen that I acquires electrons while Pb loses electrons.

Phonon dispersion and vibrational properties

The investigation of the electron–phonon coupling mechanism in BA_2PbI_4 is crucial to better understand the material's poten-tial application in photoelectric devices. Fig. 6(a)–(f) show the phonon dispersion curves and phonon vibrational density of states (VDOS) of BA_2PbI_4. The whole frequency domain range of VDOS is from $-50\ cm^{-1}$ to $3300\ cm^{-1}$, which is divided into three typical regions of phonon modes, low frequency from $-50\ cm^{-1}$ to $500\ cm^{-1}$, intermediate frequency from $500\ cm^{-1}$ to $2500\ cm^{-1}$, and high frequency from $2500\ cm^{-1}$ to $3300\ cm^{-1}$. The combination of partial VDOSs from different material components and atomistic interaction types contrib-utes to the overall VDOS. In Fig. 6(c), the main peaks of inter-mediate frequency and high frequency modes in the phonon dispersion curves and VDOS are contributed by the vibration of different bond atoms (bond stretching, angular bending, and dihedral rotation) in the BA^+ cation. For example, the C–H
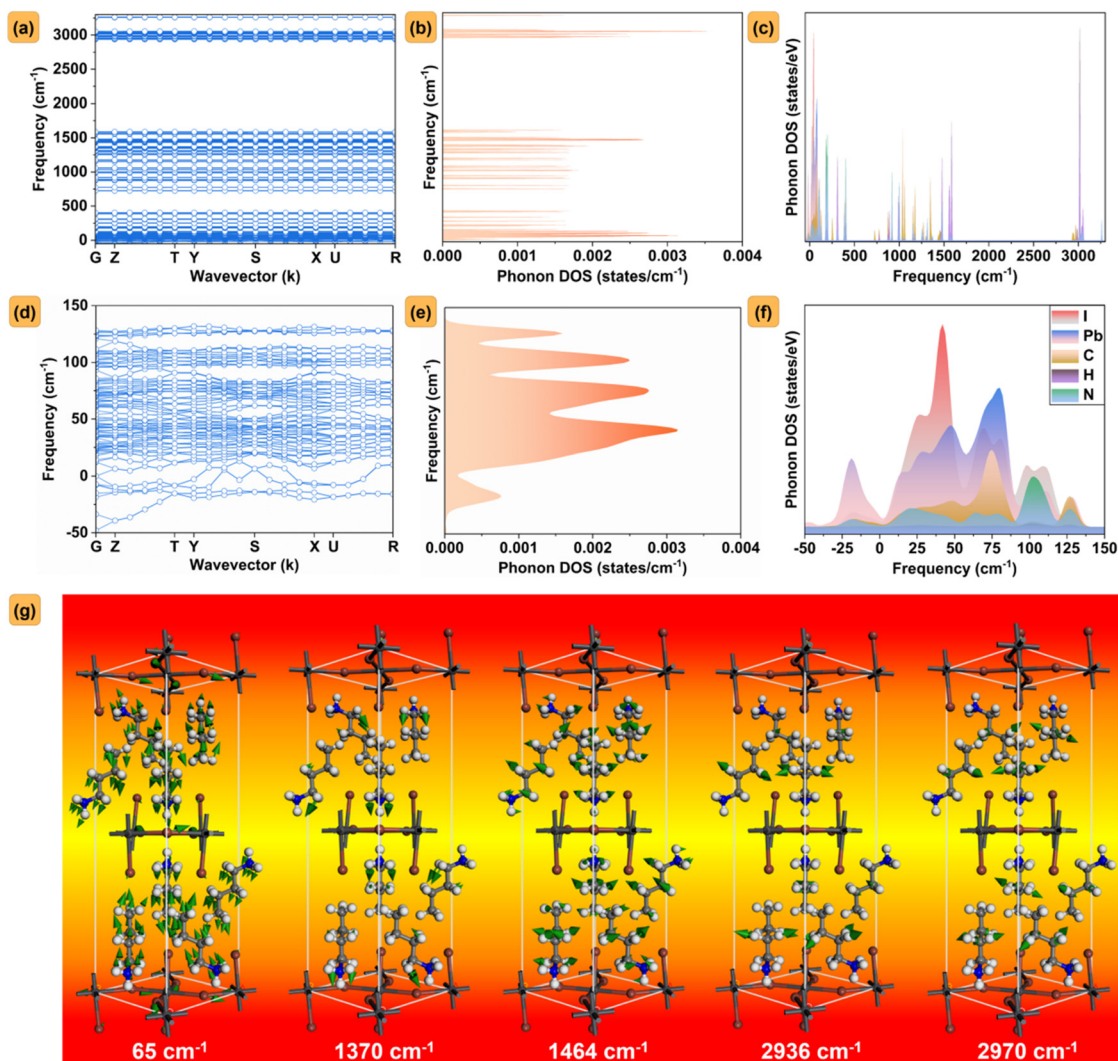
Fig. 6 (a) and (d) Phonon dispersion curves, (b) and (c) VDOSs, and (e) and (f) low frequency VDOSs of BA_2PbI_4. (g) Vibration of phonon modes in BA_2PbI_4. Green arrows represent the atomic vibration direction.

and N–H bond interactions are stiff peaks in the high frequency mode, and the C–N bond interactions are less stiff peaks in the intermediate frequency mode. In contrast, the main peak in the low-frequency modes is due to the weak interaction within the ion PbI_3^- structure and the coupling ion interaction between BA^+ and PbI_3^-. As shown in Fig. 6(g), these are several typical vibration modes, which are consistent with the FTIR spectra results of previous studies.[27]

Optical properties and contactless testing device

As shown in Fig. 7(a), the ratio of the two emission peaks (520 nm and 564 nm) of the PL spectra of BA_2PbI_4 crystals changes under different angles of excitation. This may originate from the double band gap, as shown in Fig. 7(b). The band gap is an important characteristic parameter of the host of luminescent materials. To approximately determine the absorption edge from the obtained diffuse reflectance spec-

trum of the host, the Kubelka–Munk absorption coefficient (K/S) relationship is used and presented in eqn (5):[28]

$$(\alpha h\nu)^2 = E_D(h\nu - E_{opt}) \tag{5}$$

where α is the optical absorption coefficient, h is the Planck constant, ν is the frequency of the incident photon, E_D is a constant, and E_{opt} is the direct band gap. As shown in Fig. 7(f), the band gap and sub-band gap energies of BA_2PbI_4 crystals are about 2.25 eV and 2.46 eV, which are consistent with the results of previous studies.[29,30] Previous studies illustrate that this comes from the different penetration depths of the stimulated light probe at different angles, which leads to different luminescences of the bulk and surface.[20,21] In order to verify this conclusion, a contactless fixed-point excitation luminous detector is designed based on the principle of an electromagnetic induction coil, as shown in Fig. 7(c). Under the magnetic field, through the principle of tip discharge (the local electric
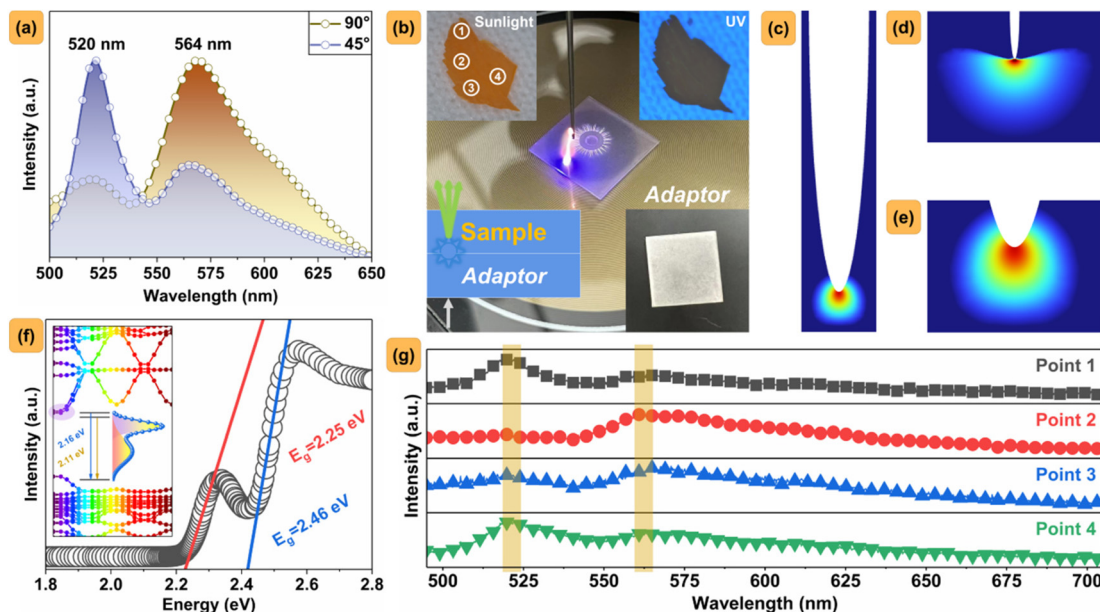
Fig. 7 (a) PL spectra with two different excitation angles. (b) A device of contactless fixed-point excitation luminescence detection. (c), (d) and (e) Electric field of tip fixed point discharge. (f) Tauc plots of BA_2PbI_4 crystals. (g) PL spectra of four points detected.

field is shown in Fig. 6(e)), the "adaptor" (LED epitaxial wafer) is excited, and the excited electroluminescence of the "adaptor" emits blue light. The blue light fixedly excites the sample, which is then collected using the spectrometer. By selecting four points on the BA_2PbI_4 crystals with different thicknesses for contactless lighting, the PL spectra collected are shown in Fig. 7(d). It can be clearly seen that the proportion of the two emission peaks has changed, which proves that the luminous peaks of the bulk and surface of BA_2PbI_4 crystals are different.

Photoelectrochemical properties

The Mott–Schottky test is commonly used to determine both the donor density and flat-band potential at the semiconductor/electrolyte interface, which is valid in the depletion zone of the semiconductor.[31] The flat-band potential (U_{fb}) and carrier density (N_d) of different optically active perovskites could be derived from Mott–Schottky analysis. The Mott–Schottky equation can be described as eqn (6):

$$\frac{1}{C^2} = \left(\frac{2}{\varepsilon\varepsilon_0 e N_d}\right)\left(U - U_{fb} - \frac{kT}{e}\right) \quad (6)$$

where C is the capacitance, ε is the dielectric constant, ε_0 is the vacuum permittivity (8.86×10^{-12} F cm^{-1}), e is the electron charge (1.602×10^{-19} C), N_d is the charge carrier concentration (m^{-3}), V is the applied potential (V), V_{fb} is the flat band potential (V), k is the Boltzmann constant (1.38×10^{-23} J K^{-1}), and T is the absolute temperature (K). As illustrated in Fig. 8(a), the Mott–Schottky plots of BA_2PbI_4 crystals shows a positive slope, which represents a typical n-type semiconductor.[28,32] The flat-band potential of BA_2PbI_4 crystals is −0.46 V relative to the Ag/

AgCl electrode through the x-intercept of the linear section of the Mott–Schottky curve. The potentials $vs.$ Ag/AgCl were converted to the normal hydrogen potentials (NHE) using the Nernst equation (eqn (7)).[33,34]

$$V_{NHE} = V_{Ag/AgCl} + V^0_{Ag/AgCl\,vs.\,NHE} \quad (7)$$

$V^0_{Ag/AgCl\,vs.\,NHE}$ is 0.197 V at 25 °C. They were equal to −0.263 V $versus$ the normal hydrogen electrode (NHE). In general, the flat band potential is approximately equal to the CB potential for n-type semiconductors and the VB potential for p-type semiconductors, respectively.[35] Therefore, by subtracting the optical band gap (2.25 eV) from the CB, the potential of the VB of BA_2PbI_4 crystals with respect to Ag/AgCl is calculated to be 1.79 V $vs.$ Ag/AgCl.

Fig. 8(b) shows the switch curve between dark and 200 μW illumination at 0.5 V and 1.0 V bias, which demonstrates the excellent switch stability of the photodetector. Transient photocurrent response measurements were carried out to confirm the photoresponses of BA_2PbI_4 crystals. The photocurrent is mainly generated by the diffusion of photogenerated carriers, and photogenerated electrons will be finally consumed by back contact, while photogenerated holes will be captured by electron donors in the electrolyte.[36] When the light was turned on at 1.0 V, the photocurrent increased sharply to 0.76×10^{-7} A. When the light was turned off, the dark current decreased sharply to 0.36×10^{-7} A. The light current is much higher than the dark current, which indicates that the photosensitive switch has good performance.

As shown in Fig. 8(c) and (d), the EIS Nyquist plots and fitted equivalent circuit model were used to investigate the charge transfer resistance of BA_2PbI_4 crystals. The inclined
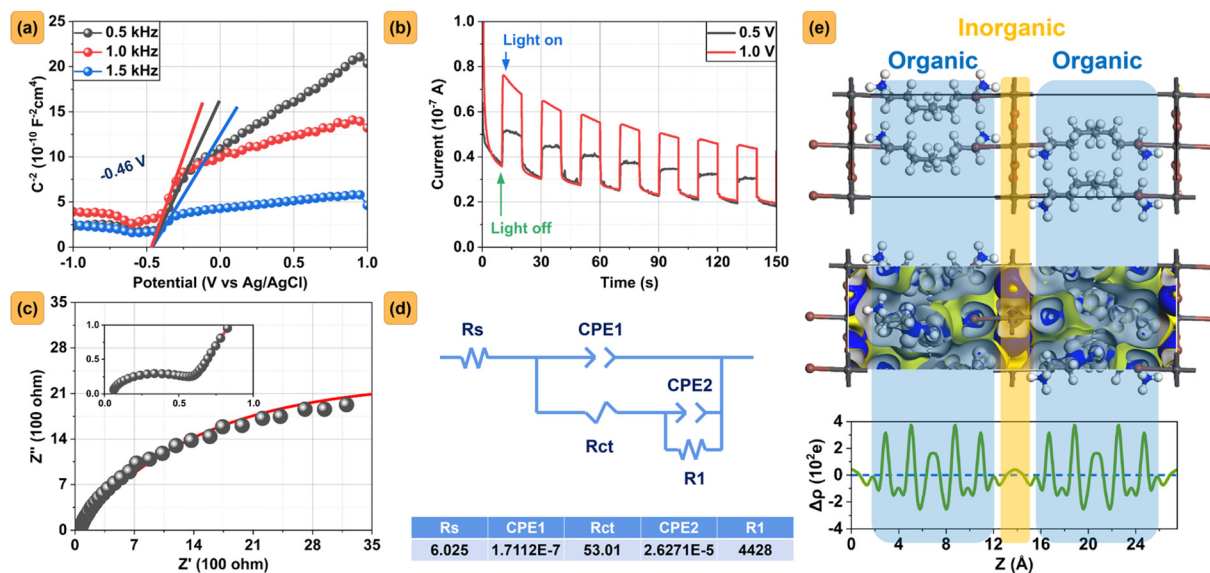
Fig. 8 (a) Mott−Schottky plots, (b) transient photocurrent responses, (c) EIS Nyquist plot, (d) fitted equivalent circuit model and (e) planar-averaged differential charge density $\Delta\rho$ of BA_2PbI_4 crystals.

straight tail appears at a lower frequency, indicating that the BA_2PbI_4 crystals have ionic transport behaviors.[37,38] BA_2PbI_4 has a "natural" quantum well structure. Early studies of organic–inorganic hybrid perovskites also provided evidence of ion conduction,[39] which is consistent with the work function study shown in Fig. 8(e). Due to the different dielectric functions of the inorganic $(PbI_6)^{4-}$ wells ($\varepsilon_W = 6.1$) and the organic $C_4H_9NH_3^+$ barrier ($\varepsilon_B = 2.1$), a self-assembled layer is formed. The huge difference of dielectric constants leads to a reduction in the shielding of the coulombic interaction between electrons and holes, which promotes the ionic transport behavior, thus leading to greater exciton binding energy.[13,40,41] This proves that the BA_2PbI_4 crystals have excel-

lent photoelectric properties and can be used in photoelectric devices, such as obtaining high conductivity light-harvesting layers in semi assembled solar cells.

Electric field simulation of different microstructures

Among previous studies, there were few studies on microstructure and photoelectric properties. In order to verify the role of the microstructure in photoelectric applications, the electric fields of spherical and cylindrical microstructures were simulated. As shown in Fig. 9, it is obvious that the electric field of the cylindrical microstructure is more uniform than that of the spherical microstructure. This ensures the stable transport of photogenerated carriers or electrons in optoelectronic appli-
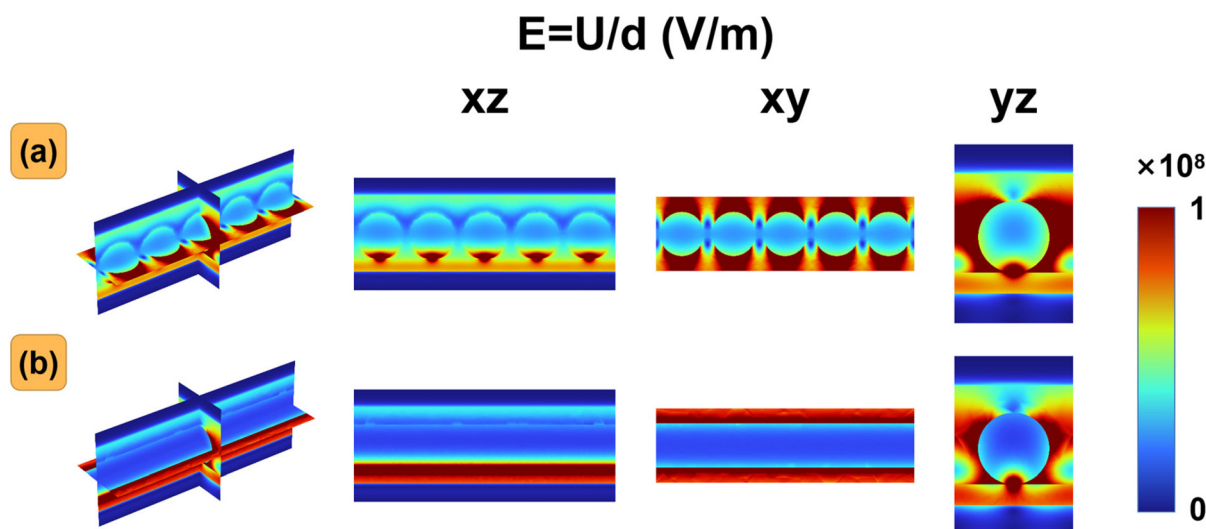
Fig. 9 Electric field under different microstructures: (a) sphere and (b) cylinder.

cations. Therefore, BA_2PbI_4 crystals with a cylindrical microstructure have excellent photoelectric properties compared with powders with a spherical microstructure.

Conclusions

In summary, BA_2PbI_4 crystals with a cylindrical microstructure were successfully prepared, and the finite element method has proved that the performance of the cylindrical microstructure in photoelectric applications is superior to that of the common spherical microstructure. The crystal structure of BA_2PbI_4 crystals was studied by the XRD of Rietveld refinement. The emission peaks of the bulk and surfaces of BA_2PbI_4 crystals were determined to be 520 nm and 564 nm using a contactless fixed-point lighting device designed with electromagnetic induction coils. The electronic structure of BA_2PbI_4 was determined using DFT calculations with the local density approximation, which was definitely assigned to the transition from the I (5p) state to the Pb (6p) state. The calculated phonon dispersion curves and vibrational properties are consistent with the existing research. The BA_2PbI_4 phase diagram of formation enthalpy was calculated. Finally, the excellent photosensitivity of BA_2PbI_4 crystals was proved by photoelectrochemical measurements, which once again proved the excellent photoelectric properties of BA_2PbI_4 crystals and the broad prospect of industrial application.

Author contributions

Conceptualization: A. D., Y. Y., E. C. and S. X.; methodology: A. D., W. Z., X. Q., D. S. and Z. L.; software: A. D. and Y. L.; validation: Y. Y. and E. C.; formal analysis: A. D.; investigation: A. D.; resources: Y. Y.; data curation: X. Q.; writing – original draft preparation: A. D.; writing – review and editing: W. Z.; visualization: A. D.; supervision: E. C. and Y. Y.; project administration: E. C. and Y. Y.; funding acquisition: T. G. All authors have read and agreed to the published version of the manuscript.

Conflicts of interest

There are no conflicts to declare.

Acknowledgements

References

1 J. H. Cai, C. H. Wang, X. P. Hu, Y. Y. Ye, L. J. Zhong, E. G. Chen, Y. Ye, S. Xu, J. Sun, Q. Yan and T. L. Guo, *Nano Res.*, 2022, **15**, 6466–6476.

2 X. X. Ren, X. Zhang, H. X. Xie, J. H. Cai, C. H. Wang, E. G. Chen, S. Xu, Y. Ye, J. Sun, Q. Yan and T. L. Guo, *Nanomaterials*, 2022, **12**, 2243.

3 C. H. Wang, J. H. Cai, Y. Y. Ye, X. P. Hu, L. J. Zhong, H. X. Xie, E. G. Chen, Y. Ye, S. Xu, J. Sun, Q. Yan and T. L. Guo, *Nanophotonics*, 2022, **11**, 1355–1366.

4 S. Ghimire and C. Klinke, *Nanoscale*, 2021, **13**, 12394–12422.

5 J. W. Choi, H. C. Woo, X. Huang, W. G. Jung, B. J. Kim, S. W. Jeon, S. Y. Yim, J. S. Lee and C. L. Lee, *Nanoscale*, 2018, **10**, 13356–13367.

6 J. Ali, Y. Li, P. Gao, T. Hao, J. Song, Q. Zhang, L. Zhu, J. Wang, W. Feng, H. Hu and F. Liu, *Nanoscale*, 2020, **12**, 5719–5745.

7 Y. Ma, P. M. Hangoma, W. I. Park, J. H. Lim, Y. K. Jung, J. H. Jeong, S. H. Park and K. H. Kim, *Nanoscale*, 2018, **11**, 170–177.

8 G. Jin, T. Liu, Y. Li, J. Zhou, D. Zhang, P. Pang, Z. Ye, Z. Xing, G. Xing, J. Chen and D. Ma, *Nanoscale*, 2022, **14**, 919–929.

9 Y. Q. Zhao, Q. R. Ma, B. Liu, Z. L. Yu, J. Yang and M. Q. Cai, *Nanoscale*, 2018, **10**, 8677–8688.

10 C. Liang, D. Zhao, Y. Li, X. Li, S. Peng, G. Shao and G. Xing, *Energy Environ. Mater.*, 2018, **1**, 221–231.

11 L. Y. Pan, Y. F. Ding, Z. L. Yu, Q. Wan, B. Liu and M. Q. Cai, *J. Power Sources*, 2020, **451**, 227732.

12 H. Tsai, W. Nie, J. C. Blancon, C. C. Stoumpos, R. Asadpour, B. Harutyunyan, A. J. Neukirch, R. Verduzco, J. J. Crochet, S. Tretiak, L. Pedesseau, J. Even, M. A. Alam, G. Gupta, J. Lou, P. M. Ajayan, M. J. Bedzyk and M. G. Kanatzidis, *Nature*, 2016, **536**, 312–316.

13 T. Ishihara, J. Takahashi and T. Goto, *Phys. Rev. B: Condens. Matter Mater. Phys.*, 1990, **42**, 11099–11107.

14 M. Y. Zhu, P. He, X. L. Yang, G. Z. Hui, C. C. Tang, G. F. Pan and L. J. Bie, *Rare Met.*, 2020, **40**, 1571–1577.

15 A. M. Tirmzi, R. P. Dwyer, F. Jiang and J. A. Marohn, *J. Phys. Chem. C*, 2020, **124**, 13639–13648.

16 L. Dou, A. B. Wong, Y. Yu, M. L. Lai, N. Kornienko, S. W. Eaton, A. Fu, C. G. Bischak, J. Ma, T. Ding, N. S. Ginsberg, L. W. Wang, A. P. Alivisatos and P. D. Yang, *Science*, 2015, **349**, 1518–1521.

17 D. Wang, B. Wen, Y. N. Zhu, C. J. Tong, Z. K. Tang and L. M. Liu, *J. Phys. Chem. Lett.*, 2017, **8**, 876–883.

18 L. Ma, J. Dai and X. C. Zeng, *Adv. Energy Mater.*, 2016, **7**, 1601731.

19 M. G. Ju, J. Dai, L. Ma and X. C. Zeng, *Adv. Energy Mater.*, 2017, **7**, 1700216.

20 T. Sheikh, A. Shinde, S. Mahamuni and A. Nag, *ACS Energy Lett.*, 2018, **3**, 2940–2946.

21 Q. Du, C. Zhu, Z. Yin, G. Na, C. Cheng, Y. Han, N. Liu, X. Niu, H. Zhou, H. Chen, L. Zhang, S. Jin and Q. Chen, *ACS Nano*, 2020, **14**, 5806–5817.

22 J. P. Perdew, K. Burke and M. Ernzerhof, *Phys. Rev. Lett.*, 1996, **77**, 3865–3868.

23 A. Biswas, R. Bakthavatsalam and J. Kundu, *Chem. Mater.*, 2017, **29**, 7816–7825.

24 E. Amerling, S. Baniya, E. Lafalce, C. Zhang, Z. V. Vardeny and L. Whittaker-Brooks, *J. Phys. Chem. Lett.*, 2017, **8**, 4557–4564.

25 D. G. Billing and A. Lemmerer, *Acta Crystallogr., Sect. B: Struct. Sci.*, 2007, **63**, 735–747.

26 M. Faizan, K. C. Bhamu, G. Murtaza, X. He, N. Kulhari, M. M. Al-Anazy and S. H. Khan, *Sci. Rep.*, 2021, **11**, 6965.

27 M. M. Rashad, A. M. Elseman and A. M. Hassan, *Optik*, 2016, **127**, 9775–9787.

28 Y. Q. He, H. Rao, K. P. Song, J. X. Li, Y. Yu, Y. Lou, C. G. Li, Y. Han, Z. Shi and S. H. Feng, *Adv. Funct. Mater.*, 2019, **29**, 1905153.

29 M. Menahem, Z. Dai, S. Aharon, R. Sharma, M. Asher, Y. Diskin-Posner, R. Korobko, A. M. Rappe and O. Yaffe, *ACS Nano*, 2021, **15**, 10153–10162.

30 L. Ni, U. Huynh, A. Cheminal, T. H. Thomas, R. Shivanna, T. F. Hinrichsen, S. Ahmad, A. Sadhanala and A. Rao, *ACS Nano*, 2017, **11**, 10834–10843.

31 A. G. Muñoz, *Electrochim. Acta*, 2007, **52**, 4167–4176.

32 H. M. Fang, J. J. Cai, H. J. Li, J. M. Wang, Y. T. Li, W. Zhou, K. K. Mao and Q. F. Xu, *ACS Appl. Energy Mater.*, 2022, **5**, 8232–8240.

33 Y. Fujii, D. Ramirez, N. C. Rosero-Navarro, D. Jullian, A. Miura, F. Jaramillo and K. Tadanaga, *ACS Appl. Energy Mater.*, 2019, **2**, 6569–6576.

34 G. F. Samu, A. Balog, F. De Angelis, D. Meggiolaro, P. V. Kamat and C. Janaky, *J. Am. Chem. Soc.*, 2019, **141**, 10812–10820.

35 H. Liu, J. Z. Li, P. Li, G. Z. Zhang, X. Xu, H. Zhang, L. F. Qiu, H. Qi and S. W. Duo, *Acta Chim. Sin.*, 2021, **79**, 1293–1301.

36 H. N. Ge, F. Y. Xu, B. Cheng, J. G. Yu and W. Ho, *ChemCatChem*, 2019, **11**, 6301–6309.

37 T. J. Ou, C. L. Liu, H. C. Yan, Y. H. Han, Q. L. Wang, X. Z. Liu, Y. Z. Ma and C. X. Gao, *Appl. Phys. Lett.*, 2019, **114**, 062105.

38 J. Q. Wang, H. Z. Shen, J. Z. Li, W. C. Li, C. Fang, J. Q. Ma, X. Cheng and D. H. Li, *Appl. Phys. Lett.*, 2020, **116**, 051102.

39 A. Ramli, M. N. A. Bakar, N. Osman, W. I. N. W. Ismail and S. Sepeai, *Mater. Lett.*, 2018, **227**, 62–65.

40 K. Tanaka, T. Takahashi, T. Kondo, T. Umebayashi, K. Asai and K. Ema, *Phys. Rev. B: Condens. Matter Mater. Phys.*, 2005, **71**, 045312.

41 K. Tanaka, T. Takahashi, T. Kondo, K. Umeda, K. Ema, T. Umebayashi, K. Asai, K. Uchida and N. Miura, *Jpn. J. Appl. Phys.*, 2005, **44**, 5923–5932.